Actin Assembly at Model-Supported Lipid Bilayers

George R. Heath, Benjamin R. G. Johnson, Peter D. Olmsted, Simon D. Connell, and Stephen D. Evans*
School of Physics and Astronomy, University of Leeds, Leeds, United Kingdom

ABSTRACT We report on the use of supported lipid bilayers to reveal dynamics of actin polymerization from a nonpolymerizing subphase via cationic phospholipids. Using varying fractions of charged lipid, lipid mobility, and buffer conditions, we show that dynamics at the nanoscale can be used to control the self-assembly of these structures. In the case of fluid-phase lipid bilayers, the actin adsorbs to form a uniform two-dimensional layer with complete surface coverage whereas gel-phase bilayers induce a network of randomly oriented actin filaments, of lower coverage. Reducing the pH increased the polymerization rate, the number of nucleation events, and the total coverage of actin. A model of the adsorption/diffusion process is developed to provide a description of the experimental data and shows that, in the case of fluid-phase bilayers, polymerization arises equally due to the adsorption and diffusion of surface-bound monomers and the addition of monomers directly from the solution phase. In contrast, in the case of gel-phase bilayers, polymerization is dominated by the addition of monomers from solution. In both cases, the filaments are stable for long times even when the G-actin is removed from the supernatant—making this a practical approach for creating stable lipid-actin systems via self-assembly.

INTRODUCTION

The actin cytoskeleton is a dynamic structure involved in cell motility, mechanical stability, and cell division (1–4). It is formed by the assembly of actin monomer units into filaments that can interact in a variety of ways, via the various actin binding proteins that cap, cut, cross-link, bundle, branch, and move actin filaments, to produce networks and bundles, depending on their cellular role (5). Consequently, they have an important role in the formation of a wide variety of biostructures, from filopodia to microvilli (6,7). Recently, a number of biological macromolecules including actin have been used to create nanoscale devices as templates for nanowires and computing (8,9). Harnessing the diverse functionality of actin and its related actin-binding proteins comprises a fast-growing area of study, producing many interesting constructs such as those utilizing myosin motors to transport cells and other cargo (10). However, our ability to easily spatially control assembly of biological macromolecules limits the complexity of possible bioconstructs and nanoscale devices.

Here we investigate lipid-induced polymerization on cationic-lipid-containing bilayers using AFM and QCM-D under a range of different lipid and buffer conditions, and in doing so describe what we believe to be a new, accessible method for generating spatially localized actin-membrane structures. In particular, we have investigated the role of pH and lipid mobility on filament growth and nucleation. Polymerization dynamics were visualized both with atomic force microscopy (AFM), allowing in-situ visualization of the slow growth of individual filaments, and with quartz-crystal microbalance with dissipation monitoring (QCM-D), giving high time-resolution but averaged over a macroscopic area of the surface. The process of polymerization was modeled to investigate whether monomers associate via two-dimensional diffusion, on the membrane, or bind directly from solution. Our model shows that in the case of fluid membranes, actin adsorption is followed via diffusion of the actin-plus-associated lipid these structures are free to diffuse until they meet a growing end on a preexisting filament of another actin to nucleate growth. In the gel phase, where diffusion is retarded, growth occurs at random points via adsorption from the solution phase and with relatively little opportunity for filaments to align.

In the presence of the nucleotide ATP, and salts such as $MgCl_2$, G-actin monomers will aggregate and nucleate the growth of the double-helical filamentous actin (F-actin) if their concentration is sufficiently high (typically $>0.1\ \mu M$). It has been shown that actin polymerization can also be induced at lipid membrane surfaces under nonpolymerizing conditions, provided the lipid membrane contains charged lipids, or surfactants, to nucleate filament formation (1,3). Renault et al. (3) showed that actin could be polymerized, under nonpolymerizing conditions beneath Langmuir monolayers of Egg phosphatidylcholine containing 25% charged surfactant (stearylamine). Transmission electron microscopy data of films transferred to grids showed mostly the formation of dense structures consisting of highly aligned filaments, i.e., paracrystals, with single filaments only being obtained under turbulent flow conditions (3). The formation of actin paracrystals from nonpolymerizing bulk was first observed by Laliberte and Gicquaud (1) on liposomes containing varying fractions of stearylamine, showing that the

Submitted July 22, 2013, and accepted for publication October 8, 2013.

*Correspondence: s.d.evans@leeds.ac.uk

Editor: Simon Scheuring.

0006-3495/13/11/2355/11 $2.00

http://dx.doi.org/10.1016/j.bpj.2013.10.007

actin layer depolymerized if the liposomes were solubilized with Triton-X. Although these studies demonstrated the formation of paracrystals on fluid bilayer surfaces, the mechanism for charged-lipid induced nucleation is not well understood. More recently, attempts to create more-complex structures based on actin architectures have utilized electrostatic self-assembly of F-actin and charged lipid membranes to form either complex multilayered tubular structures (11) or three-dimensional crystallization of fluorescent quantum dots within a stacked actin-lipid membrane template (12).

The planar nature of supported lipid bilayers makes them ideal for investigating dynamic processes at the subnanometer scale. Previous studies of actin/bilayer interactions have focused on the addition of prepolymerized filaments to supported bilayers. G-actin and F-actin binding to Egg-phosphatidylcholine bilayers through the transmembrane protein ponticulin was achieved by Barfoot et al. (13). Shi et al. (14) used electrostatic binding of F-actin on charged lipid bilayers to form actin paracrystals, the tight packing allowing single-actin monomers to be directly resolved by AFM in the contact mode. Alternative techniques for forming actin layers have utilized intermediary linkers; for example, biotinylated G-actin has been used as a nucleator for filament formation when attached via streptavidin, and actin binding proteins with an additional His tag to link actin to Ni-NTA tagged lipids (15–18).

The dynamics of actin polymerization have been extensively studied with a variety of fluorescence techniques in bulk and at liposome surfaces (18–20), but to our knowledge, there have only been two high-resolution AFM studies. Using HeLa cell extracts on mica, Lehto et al. (21) imaged actin polymerization after adsorbing endosomes followed by addition of cytosol from the HeLa cells. More recently, high-speed AFM techniques were used to study the process of polymerization of actin onto biotinylated-actin nucleation sites attached to a two-dimensional streptavidin crystal. In this study, high imaging forces could be used to break the filament to simultaneously observe growth at both the barbed and pointed ends of the F-actin filament, with data showing addition of either monomers or dimers at rates comparable to bulk studies (15).

MATERIALS AND METHODS

Materials

The lipids used throughout were DPPC (1,2-dipalmitoyl-*sn*-glycero-3-phosphocholine), EDPPC (16:0) (1,2-dipalmitoyl-*sn*-glycero-3-ethylphosphocholine, positively charged), DOPC (1,2-dioleoyl-*sn*-glycero-3-phosphocholine), and DOTAP (1,2-dioleoyl-3-trimethylammonium-propane, positively charged), all purchased from Avanti Polar Lipids (Alabaster, AL). All lipids were dissolved in 50:50 chloroform/methanol. Rabbit skeletal muscle actin was purified from rabbit muscle acetone powder following previous methods (Pardee and Spudich (22)). Its purity was checked by sodium dodecyl-sulfate polyacrylamide gel electrophoresis, and its concentration was determined by a bicinchoninic acid assay (23). Stored at −80°C, the G-actin solution was diluted to the desired working concentration of 0.04 mg/mL in G-buffer (5 mM Tris-HCl pH 7.5, 0.02 mM $CaCl_2$, 0.2 mM ATP, and 0.5 mM DTT). After 30 min at 4°C, the diluted actin was then centrifuged (100,000*g*, 4°C, 1 h) to remove any large actin crystals generated by the snap-freezing process. The supernatant was collected and diluted in buffer (5 mM Tris-HCl pH 7.5, 2 μM $CaCl_2$, 20 μM ATP, and 50 μM DTT) at 0.04 mg/mL ready for use in G-actin experiments.

Supported lipid bilayer formation

Supported lipid bilayers were formed using the vesicle rupture method. Lipid mixtures were first dried in a vial using a steady stream of zero-grade nitrogen, following which they were maintained under vacuum for several hours. The dried lipids were then hydrated with Milli-Q water (Millipore, Billerica, MA) to a final lipid concentration of 0.2 mg/mL. This suspension was then tip-sonicated for ~10 min, until clear. One-hundred microliters of this solution was added to a freshly cleaved mica substrate where the bilayer forms through incubation of the lipid. If the samples contained lipids with phase-transition temperatures above 25°C, they were incubated in a sealed humid chamber within an oven at 50°C for 20 min. Other lipid mixtures were incubated at room temperature. Finally, the bilayers were rinsed several times directing the flow parallel to the surface to remove any unruptured vesicles weakly attached to the substrate and remaining in solution. Rinsing involved 10 repeat washes, each with ~100 μL of buffer from a Gilson pipette. The hydrated bilayer was then carefully inserted into the AFM.

AFM imaging and analysis

AFM experiments were performed at room temperature (22°C) using a Multimode 8 AFM on a NanoScope V controller (both by Bruker Daltonics, Billerica, MA). Oxide-sharpened silicon nitride tips (Bruker Daltonics) with typical spring constants of 0.32 N/m were used in either tapping mode or peak-force tapping mode. All images were performed on mica substrates mounted on Teflon (E.I. du Pont de Nemours, Wilmington, DE) disks in G-buffer conditions. Filament surface coverage was calculated using a bearing analysis. To avoid miscalculation caused by tip convolution, filament density and filament packing fraction were determined by importing images into the software IMAGEJ (National Institutes of Health, Bethesda, MD) and manually tracing individual filaments with segmented lines. Summed lengths of all filaments were converted to an area or packing fraction by assuming a constant filament thickness of 7.5 nm.

QCM-D

QCM-D measurements were performed using a model No. E4 multifrequency QCM-D instrument (Q-Sense, Gothenburg, Sweden) in a flow-through cell of 40 μL volume. Data from 15, 25, 35, 45, 55, and 65 MHz overtones (third, fifth, seventh, ninth, 11th, and 13th, respectively) were collected. Before use, all SiO_2 crystals were cleaned by ultrasonication in 0.4% sodium dodecyl-sulfate for 15 min followed by copious rinsing and ultrasonication in Milli-Q water for 15 min. The crystals were then dried under nitrogen and UV-ozone cleaned for 30 min. After UV-ozone treatment, they were rinsed with Milli-Q water, dried under nitrogen, and used immediately. Initially, the system was filled with buffer such that the resonant frequencies of the overtone to be used could be found. The vesicle solution was injected, under a constant flow of 40 μL/min, at a concentration of 0.1 mg/mL. Frequency and dissipation changed in a manner characteristic of vesicle adsorption and then rupture, to form a planar bilayer. Upon reduction of the dissipation peak to a minimum, indicating complete bilayer formation, the bilayer was rinsed with Milli-Q water and then with buffer to remove adhering vesicles. After bilayer formation, G-actin was added at 14 μL/min and changes in frequency and dissipation were monitored. The actin layer was modeled using the software QTOOLS (QSense) with a Kelvin-Voigt model and a minimum of three overtones.

RESULTS AND DISCUSSION

Actin adsorption and polymerization on fluid-phase lipid bilayers

The interaction of G-actin, under nonpolymerizing conditions, with DOPC/DOTAP lipid bilayers was investigated using AFM and QCM-D. The concentration of the cationic lipid DOTAP was varied between 0 and 30% mole fraction. G-actin was introduced at 0.1 μM and incubated for 10 min. In all cases, the bilayers were featureless before the introduction of actin, as shown in Fig. 1 *A*. Force spectroscopy was used to establish the bilayer thickness/integrity, before G-actin addition, by pushing the tip through the lipid bilayer. For a good bilayer, not only was the image uniform but, as the AFM tip penetrated the bilayer and came into contact with the underlying mica surface, the push-through displayed a characteristic 5-nm jump in the approach curves (*inset*, Fig. 1 *B*).

For pure DOPC bilayers, there was no adsorption of G-actin (Fig. 1 *A*). However, as the fraction of DOTAP was increased to between 0.5 and 12.5%, the adsorption of a small number of G-actin monomers was observed. Fig. 1 *C* shows a G-actin density of ~4 μm^{-2} on a 5% DOTAP surface; this value is much lower than the surface charge would allow (~10^4 μm^{-2} based on seven charged lipids per G-actin) and may only reflect an immobile fraction of G-actin. Total internal reflection fluorescence (TIRF) microscopy image sequences (see Fig. S1 and Movie S1 in the Supporting Material) show the presence of both mobile and immobile fractions of G-actin. It seems probable that, in AFM, one images the immobile fraction but not the highly mobile fraction, which has an average diffusion coefficient of 2.2 $\pm$ 1.1 $\mu m^2/s$. The TIRF data also shows an immobile fraction of actin as observed in the AFM. Although the exact mechanism to explain why some actins are mobile when other actins are not is still an open question, it might reflect the number of lipids binding per G-actin monomer. We would envisage a dramatic reduction on the monomer diffusion coefficient when it is bound to multiple lipids than, say, when it is bound to a single lipid. Height analysis of the immobile bound G-actin gives peaks at 3.5 $\pm$ 0.3 and 5.3 $\pm$ 0.6 nm (Fig. 1 *C*, *inset*), i.e., consistent with the dimensions of G-actin (3.5 $\times$ 5.5 $\times$ 5.5 nm) obtained from structural models (24). The peak at smallest dimension of 3.5 nm is dominant, and suggests the monomers preferentially lie flat to optimize interaction with the bilayer.

At 15% DOTAP, loosely bound or possibly highly mobile single-filament features were observed, indicating a critical threshold had been passed for nucleation of filament growth. For DOTAP concentrations >18%, a near-complete monolayer of ordered F-actin filaments was formed (Fig. 1 *D*), although there was still no evidence of polymerization in the bulk. This sharp transition from almost no coverage to a full monolayer suggests that there is a critical threshold for polymerization or, possibly, that the charge presented in the outer bilayer leaflet may change abruptly above certain critical concentration. Previous work on binding prepolymerized filaments to charged membranes does not appear to show this same critical threshold effect (11,12,14,25). The surface coverage on the 20% DOTAP samples was estimated, using bearing analysis, to be between 97 and 100%. However, the packing fraction defined as the ratio of the filament diameter/average

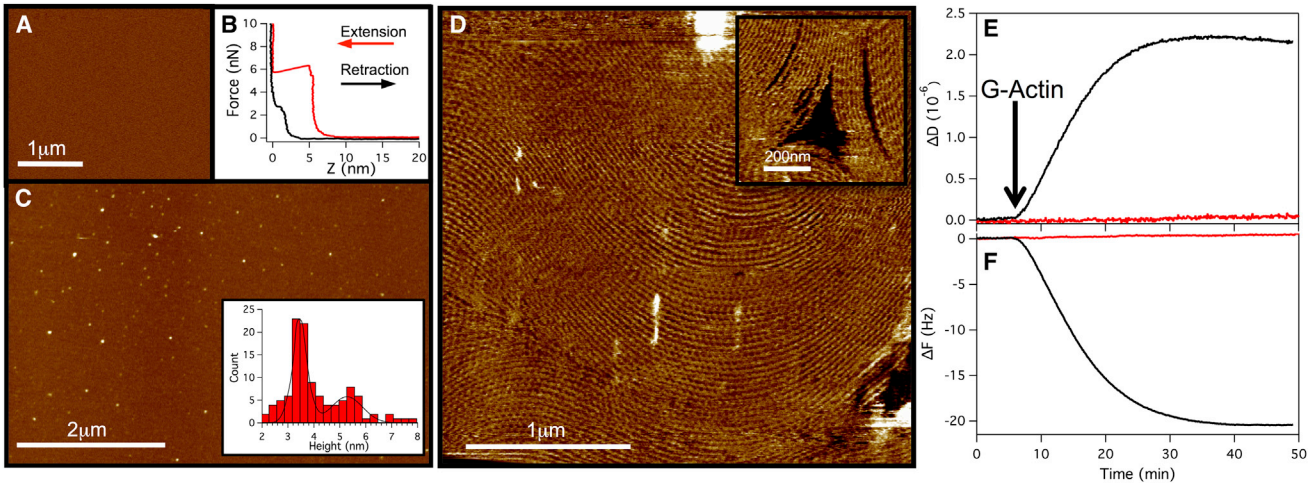

FIGURE 1 (*A*) AFM image of pure DOPC bilayer after incubation with G-actin showing no measurable nonspecific adsorption. (*B*) Force spectroscopy measurement of panel *A* showing bilayer break-through event. AFM images after incubation with G-actin (*C*) DOPC + 5% DOTAP (*inset*: histogram of particle height from four different 10-μm scan areas) and (*D*) DOPC + 20% DOTAP (*inset*: liquid crystal defect). The average filament separation in panel *D* ranges from 22 nm for straight filaments up to 41 nm for those in high-curvature regions. All images obtained under G-buffer conditions (Z scale = 6 nm, scale bars = 1 μm). QCM-D showing changes in dissipation (*E*) and frequency (*F*) during incubation with 0.1 μM G-actin with DOPC (*red*) and a 4:1 DOPC/DOTAP (*black*) bilayers. To see this figure in color, go online.

distance between neighboring filaments ranges from to 0.5 for parallel filaments to 0.22 for areas with high curvature, as shown in Fig. 1 *D*.

Observation of polymerization dynamics with AFM was problematic because the filaments appeared to be highly mobile and grew too quickly. Therefore, QCM-D was used to follow the adsorption kinetics of G-actin on pure DOPC and DOPC lipid bilayers containing 20% DOTAP (Fig. 1, *E* and *F*). As observed in the AFM experiments, pure DOPC bilayers showed no adsorption of G-actin, hence confirming that the interaction is purely electrostatic. The 20% DOTAP bilayer showed large changes in both frequency and dissipation until saturation is observed after ~30 min. The change in frequency with time could be fit to an exponential with a time constant of 570 ± 10 s. Previous studies on the kinetics of G-actin adsorption to lipid monolayers containing charged surfactant found similar exponential behavior using ellipsometry but at slower rates with time constants of ~1800 s (3). This difference can be partially explained by this previous study having used a lower actin concentration (0.06 μM, compared to 0.1 μM used here) and using different lipids. Modeling the dissipation and frequency curves as a two-layered Kelvin-Voigt model (see the Supporting Material), with the bilayer as the first layer and assumed to be constant over time, gave an actin layer thickness of 3.3 ± 0.2 nm. Converting the volume of this single uniform layer to rods formed from uniform spheres with a 3.75-nm radius gives a packing fraction of 0.56 ± 0.03, which is in reasonable agreement with our AFM observations of actin polymerization on fluid-phase bilayers.

We assume that the actin monomers, when bound to a charged lipid or lipids, will have a larger residency time on the surface, coupled with the reduced dimensions for two-dimensional diffusion in the plane of the membrane leading more readily to dimer formation as the precursor to filament formation (26). The mobility of the DOTAP/actin complexes allows the filaments to align during growth to form fingerprint textures similar to those observed in calamitic liquid crystals (27). The almost-complete surface coverage has some topological defects characteristic of liquid crystals, with evidence of disclination lines and ±1/2 type defects (Fig. 1 *D* and its *inset*).

In some regions, highly ordered bright lines were observed to run perpendicular to the filament direction (Fig. 2 *A*), representing paracrystal formation. The bright bands appear due to the alignment of the actin repeat units in neighboring filaments. Fig. 2 *B* shows a high-resolution image of such a paracrystalline region. The filaments lie in the direction shown by the red line, which gives the characteristic profile (Fig. 2 *D*) with a 3-nm half-helical repeat as expected for actin (28). The blue-line traces perpendicular to the filaments provide a measure of the interfilament spacing, estimated to be 19 ± 1.1 nm (Fig. 2 *C*). The formation of paracrystals is expected to occur after the polymerization process, because filaments reorient on the fluid membrane into configurations that are the most favorable in terms of lateral electrostatic interactions of filaments. Previous studies of prepolymerized filaments support this dependence on membrane fluidity, showing the formation of actin paracrystals on fluid-phase but not gel-phase membranes (25).

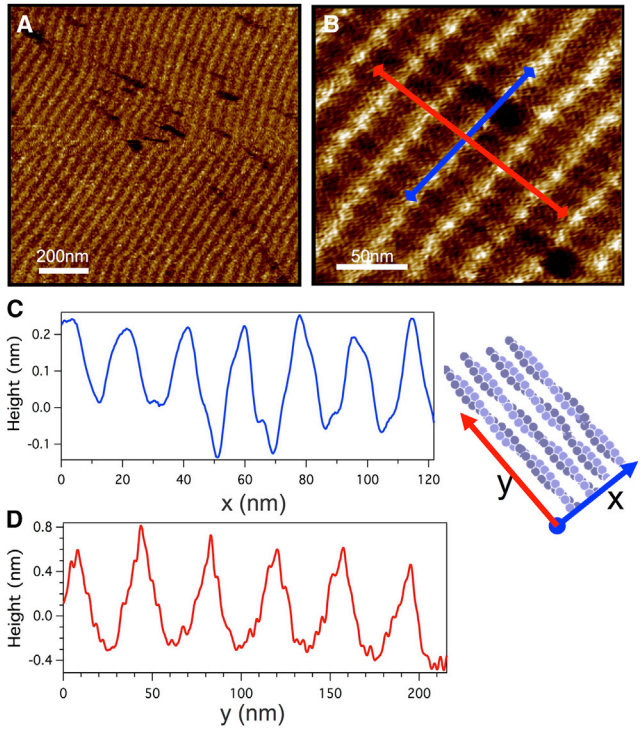

FIGURE 2 (*A*) AFM data showing surface topography of actin paracrystals polymerized on a cationic fluid lipid bilayer (DOPC with 20% DOTAP) in G-buffer conditions. (*B*) High-resolution scan showing the individual filaments within the paracrystal; the visible periodicity is caused by the alignment of the helical repeats of parallel filaments. (*C* and *D*) Interfilament spacing and helical repeat in the paracrystal. To see this figure in color, go online.

The packing fraction obtained in paracrystalline regions was found to be 0.5, significantly smaller than observed for two-dimensional paracrystals prepared in polymerization buffer, which typically give a interfilament spacing of 7–8 nm (14). The packing in our system is, however, comparable to results found in transmission electron microscopy studies of actin polymerized by amine-containing lipid surfaces (3). The difference in packing between polymerization buffer and lipid-induced polymerization arises due to the lower divalent cation concentration in the nonpolymerizing buffer (0.02 mM $CaCl_2$) compared to the polymerizing buffer (2 mM $MgCl_2$). The higher concentration of divalent cations is great enough to allow binding of Mg to several low-affinity sites on F-actin (29), thus reducing the overall charge of filaments. This may then permit closer packing and allow adjacent filaments to bind to each other, as previously shown in bulk solution (30).

Actin adsorption and polymerization on gel-phase lipid bilayers

To demonstrate the importance of lipid mobility on the type of actin structures formed on polymerization, we made lipid bilayers composed of lipids that are in a gel phase at room temperature. Bilayers of DPPC (T_m = 41°C) and EDPPC (ethylphosphocholine), a cationic-headgroup-modified DPPC, were formed at 55°C and allowed to cool to room temperature before imaging. Fig. 3 *A* shows the filament structure found after the incubation, at room temperature, of a gel-phase lipid bilayer (80% DPPC, 20% EDPPC) with G-actin. Notwithstanding the presumably reduced mobility within the gel phase, polymerization was still nucleated by the charged lipids. However, the filament coverage (32 ± 2%) was significantly lower than for the fluid-phase system (>97%), and individual F-actin filaments displayed a reduced ability to reorient to achieve high-density packing. Repeating the experiment with the actin incubation at 45°C, i.e., just above the gel/fluid-phase transition for 15 min before cooling for imaging, gave a significant increase in surface coverage to 78 ± 8% (Fig. 3 *B*) and showed a return of the actin textures more closely resembling the paracrystals shown in Fig. 2. The different structures observed for actin incubation above and below the phase transition demonstrate that diffusivity of the nucleation site (in this case EDPPC/actin complex) plays a significant role in controlling morphology of the actin structures formed. We note that, for these systems, actin agglomeration (i.e., large white objects) was observed (Fig. 3 *A*), which presumably arises as a result of three-dimensional nucleation. Images of the gel-phase membrane before and after actin addition (see Fig. S2) show that these large agglomerates only appear after actin addition.

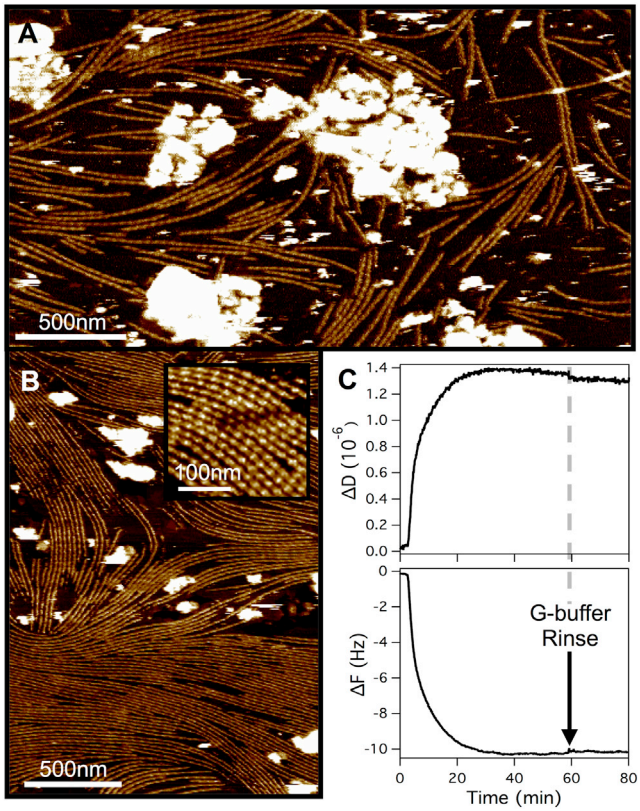

FIGURE 3 Actin polymerization on gel-phase lipid bilayers (4:1 DPPC/EDPPC). AFM image after actin incubation at room temperature (*A*) (*inset*, higher magnification image) and (*B*) after 15-min incubation at 45°C followed by 30-min cooling period (scale bars = 1 μm). (*C*) QCM-D showing changes in frequency and dissipation observed upon adding 0.1 μM G-actin to 4:1 DPPC/EDPPC lipid bilayer at room temperature and with a continual G-buffer rinsing step from 58 min onwards. To see this figure in color, go online.

To investigate the charge required to nucleate polymerization on gel-phase bilayers, we varied the EDPPC concentration in DPPC bilayers from 0 to 20%. Bilayers with 0 and 1% EDPPC showed no interaction with G-actin, whereas for 5 and 20% EDPPC, actin is polymerized to the same degree (see Fig. S3 and Fig. S4). Hence, the critical concentration of charged lipid is significantly lower than found for the fluid bilayer system (18%). This difference in critical concentration for filament nucleation may reflect differences in the lipid composition in the upper leaflet compared to the lower leaflet (adjacent to the mica surface) for the fluid- and gel-phase systems. Previous studies have shown that supported fluid lipid bilayers containing charged lipids display significant leaflet asymmetry on mica. It was found that for bilayers containing between 10 and 20% charged lipid the fraction of charged lipid in the upper leaflet compared to the lower leaflet varies from the ideal 1:1 to 1:3 (31). Because rates of flip-flop in the gel phase are orders-of-magnitude slower than for fluid systems it is reasonable to assume that the fluid system is more likely to be susceptible to lipid asymmetry than the gel. In addition, given that the lateral lipid density in the gel phase is higher than that in the fluid phase by a factor of 1.4–1.5, the gel has a higher charge density of roughly 1.4–1.5-fold (based on values for DOPC and DPPC area per headgroup (32,33)). If both of these effects are taken into account (i.e., ~50% increase in charge density plus 1:3 asymmetry in the fluid, but not the gel), then the critical composition for filament formation would change from 18% in the fluid system down to a predicted 4% for the gel-phase system. This is in good agreement with our observations of the gel system.

We also investigated the effects of increasing the EDPPC concentration above 20%; from Fig. S3, it is evident the two lipids phase-separate to form gel-phase domains with a height over the fluid phase of 1.3 ± 0.2 nm. The phase separation appears to have negligible effects on the morphology of the actin polymerized at the surface of the gel-phase domains (see Fig. S4).

The QCM-D response to G-actin incubation after forming a 20% EDPPC bilayer (Fig. 3 *C*) shows similar kinetics behavior to those observed with the fluid bilayer system.

Exponential fitting to frequency change gives a time constant of 350 s with an end-frequency change of −10.2 Hz, corresponding to a layer of filaments with packing density of 0.29. This is slightly greater than expected from AFM imaging (0.1 packing fraction). However, the AFM analysis here excludes the regions of three-dimensional growth, whereas QCM-D measures all adsorption. Once the actin filaments have formed on the surface they are not easily dislodged by washing with buffers, even those of high ionic strength (e.g., 1 M $CaCl_2$), suggesting a tight binding to the surface and thus making this system not only biologically interesting but also robust for possible applications.

Because the filament mobility on gel-phase bilayers was relatively slow, the growth of individual filaments could be visualized at standard AFM scan rates (2 Hz). This allowed various phenomena to be observed such as filament annealing, whereby two filaments associate to form one (Fig. 4 *A*). Filament annealing has been previously well studied in vitro and is believed under certain conditions to play a role in filament elongation in vivo (34,35). The contribution to filament growth by annealing, observed here, is small; however, it may play a greater role in fluid membrane systems where filament diffusion would be expected to be greater. Force generation, where polymerizing filaments can be seen to bend other obstructing filaments as they grow, was also observed (Fig. 4 *B*). Fig. 4 *C* shows the action of filament breakage, by the AFM tip, followed by growth from each of the new ends, all in the same direction. This preferential growth from the plus-end demonstrates the polarization of the actin filament whereby all subunits point toward the same filament end, and is consistent with the myosin-head-based decoration of actin filaments studied by electron microscopy (36). Tracking the filament length between AFM scans allowed determination of the filament growth rate. Fig. 4 *D* shows filament length versus time for many different single filaments (*gray*) with an averaged plotted in red. In most cases, the growth remains linear until reaching another obstructing filament at which, depending on the available space, the obstructing filament is moved or bent, as can be seen in Fig. 4 *B*. This linear growth is characteristic of filaments in bulk solution (20).

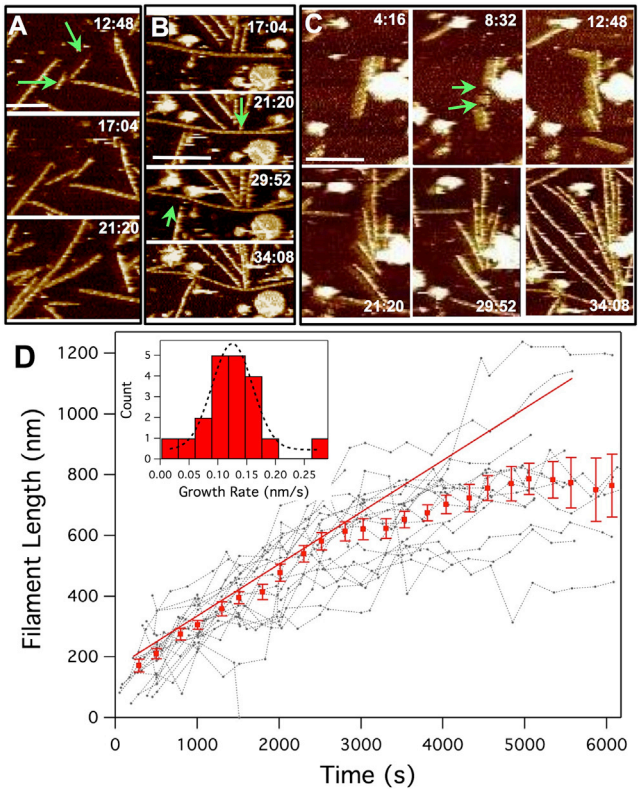

FIGURE 4 Time-lapse AFM image sequences showing: (*A*) the process of filament annealing whereby two filaments associate to form a single filament; (*B*) a filament being forced to bow by the growth of other surrounding filaments; and (*C*) a single filament being broken into smaller fragments by the AFM tip after growth from the new free ends (time stamp, min/s; scale bars = 200 nm). (*D*) Tracking filament length with time taken from a sequence of AFM images (see Movie S2 in the Supporting Material). (*Gray lines*) Individual filaments; (*red points*) average values. (*Inset*) Histogram of filament growth rates based on linear fits to changes in length over initial linear growth regime ($n = 19$ filaments). To see this figure in color, go online.

Fitting the filament length versus time plots for a number of filaments gave a distribution of filament growth rates centered at ~7.8 ± 0.7 nm/min (Fig. 4 *D*, *inset*). This rate is significantly slower than that observed under polymerizing conditions using AFM, in cell extracts on mica (91 nm/min) (21), on streptavidin substrates (110 nm/min) (15), or in bulk solution with TIRF microscopy (600 nm/min) (20).

Effect of pH on lipid-membrane-induced actin polymerization

The effect of pH on the polymerization of actin in bulk solution has been well characterized, with faster polymerization rates and a decrease in the critical concentration of G-actin required as the pH is reduced (37). The driving force for this is a reduction in the net charge per actin monomer as the pH approaches the isoelectric point, $pI = 5.5$. Excluding the acidic vesicles, the range of pH in cytoplasm is generally bounded by ~6.5–8.0 (37). Thus, we have varied the pH of the buffer between 6.5 and 7.8 and imaged the actin structures produced at room temperature on a 4:1 DPPC/EDPPC bilayer with AFM.

Time-lapse AFM imaging at various buffer pH values (Fig. 5, *A–C*, and see Movie S2, Movie S3, and Movie S4) shows the polymerization dynamics of many filaments over hours. The polymerization characteristics appear to alter with pH. At lower pH values, polymerization often nucleates along the sides of existing filaments (Fig. 5, *A* and *B*) but at pH 7.5, nucleation is random (Fig. 5 *C*). Although the data at lower pH is limited due to fast growth rates and interactions between filaments altering filament positions, it was possible to track length changes of several

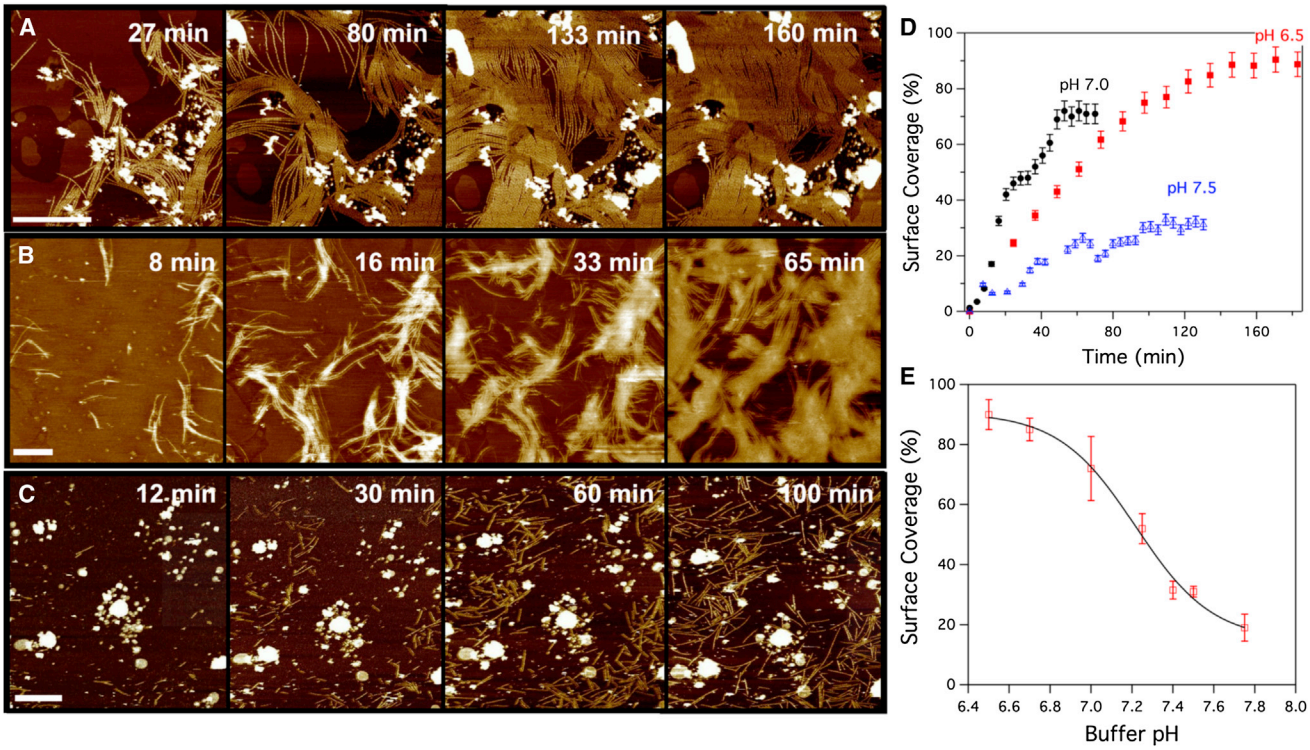

FIGURE 5 AFM image sequence of actin polymerization on a 1:4 EDPPC-DPPC bilayer in G-buffer at pH 6.5 (*A*), 7.0 (*B*), and 7.5 (*C*) (scale bars = 1 μm). (*D*) Total actin surface coverage from AFM time-lapse data as a function of time at pH 6.5 (*solid squares*), pH 7.0 (*solid circles*), and pH7.5 (*triangles*) with exponential curves fitted. (*E*) Final surface coverage of filaments as a function of buffer pH after 30 min. To see this figure in color, go online.

filaments with time. As with polymerization at pH 7.5, the filaments at pH 6.5 appear to grow linearly and with no visible loss/depolymerization from the negative end. The average growth rate of 28 $\pm$ 4 nm/min, however, is several times greater than that found at pH 7.5. The growth of multiple membrane-actin layers is observed under pH 6.5 buffer conditions, such that the polymerization of actin is drawing out lipid from the underlying bilayer (Fig. 5 *A* and see Movie S4). The time-dependent actin coverage (Fig. 5 *D*) shows that decreasing the pH from 7.5 to 6.5 leads to an increase in both the rate and amount of coverage achieved. Counts of filament number with time show that the increase in coverage observed at lower pH is not only due to increased polymerization rate but also the total number of filament nucleation events. This has been previously observed in bulk (38). Surface coverage analysis of the AFM images obtained after 30-min incubation with varying pH (Fig. 5 *E*) shows that the actin coverage increased in a sigmoidal manner from ~20 to 90% as the pH was reduced from 7.8 to 6.5. It should be noted, however, that after the 30 min, some of these systems may still be undergoing polymerization.

Fig. 6 *A* shows the frequency shift obtained in QCM-D experiments for DPPC/EDPPC bilayers with pH varying between 6.5 and 7.8. The results suggest approximately linear adsorption followed by saturation, with rates and saturation points depending on pH. As observed with the AFM, decreasing the pH led to an increase in the actin coverage as well as the rate of adsorption (Fig. 6 *B*). This is most likely due to a reduction in the electrostatic interactions both between actin monomers and between G-actin and charged lipids. As a result, fewer charged lipids are required per G-actin monomer, and the filaments polymerize more

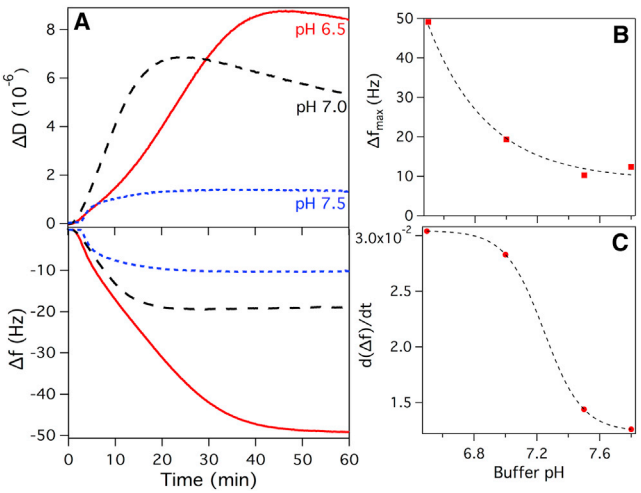

FIGURE 6 (*A*) QCM-D data showing actin adsorption on gel state 4:1 DPPC/EDPPC bilayers for buffers at pH 7.8, 7.0, and 6.5 (*blue*, *black*, and *red*). Maximum change in frequency (*B*) and adsorption rate gradient (*C*) as a function of buffer pH. To see this figure in color, go online.

readily. The saturation time was at least twofold quicker when determined by QCM-D, compared to the AFM imaging. Investigations of varying AFM scan intervals between 4 and 13 min have shown that this is not due to tip interactions, and that the difference therefore most likely arises from the different flow conditions used between the AFM (static) and QCM-D (40 μL/min), suggesting that reaction is strongly affected by diffusion.

The higher final coverage values obtained for the lower pH values is most likely due to the combination of an increased filament mobility and an increased rate of nucleation (as observed with AFM), because fewer lipids are required to bind a single filament/monomer. The dissipation provides an indication of how tightly bound the adsorbed material is, or its coupling to the aqueous phase. In all cases, the dissipation reached a maximum in line with the changes in frequency, before then decreasing while frequency remained constant, suggesting filaments may be ordering to form more tightly packed structures (or that bound g-actin may be polymerizing via two-dimensional diffusion). The high dissipation values reached for pH 6.5 and 7.0 may also be due to the formation of actin membrane multilayers as observed by AFM. It should be noted that when the changes in dissipation are relatively high, the changes in frequency do not simply reflect mass adsorption in a linear manner. The pH dependence thus provides useful insight for understanding the mechanism of actin polymerization at surfaces, which we will now discuss.

Model of lipid-charge-induced actin polymerization

Actin monomers carry a high negative charge; typically ~$-7e$ (depending on buffer conditions) and thus electrostatics play a significant role in polymerization. In bulk polymerization this charge is reduced and screened by the binding of Mg^{2+} or Ca^{2+} to a single high-affinity site and binding of Ca^{2+}, Mg^{2+}, and K^{+} to several lower-affinity sites (K_d values of 0.15 mM for Ca^{2+} and Mg^{2+} and 10 mM for K^{+}) (29). The 2 μM $CaCl_2$ used in our experiments provides a high enough concentration for Ca^{2+} binding to the single high-affinity site of G-actin without binding to the low-affinity sites. Because there is no Mg^{2+} or K^{+} in our buffers the G-actin monomers still carry a high enough negative charge to prevent polymerization in bulk. For polymerization to proceed under these conditions, the charged lipid within the bilayer must neutralize the excess charge on the actin. Previous studies of actin filaments grown at charged membranes have shown that only roughly half of the ATP bound to the F-actin subunits is hydrolyzed to ADP as opposed to the usual ~80% hydrolysis when polymerized in bulk with salts (1). This incomplete ATP hydrolysis on charged membranes suggests some direct interaction between the lipids and actin monomers. Because roughly half of the monomers of the filament are in contact with the membrane and only half of the subunits can hydrolyze their ATP, there may be a direct binding of the lipid headgroup to specific sites on the actin, which may then prevent hydrolysis. Our observations of no depolymerization or detachment after rinsing agree with this argument of direct G-actin binding to lipids, and may explain the preferential flat orientation of G-actin monomer binding observed (Fig. 1 *C*).

The charge of a G-actin monomer was estimated using the Tanford-Kirkwood method (39–42), with the MACRODOX charge set software (S. H. Northrup, K. A. Thomasson, and colleagues; http://iweb.tntech.edu/macrodox/mdxhelp/overview.html). For the pH range used in our experiments (6.5–7.8), the method predicts total charges ranging from -4.1 to -7.7. An actin monomer lying flat as AFM suggests (55×55 Å) would cover ~40 or 65 lipids on a fluid- or gel-state lipid bilayer, respectively. Therefore, an area of fluid bilayer with 20% charge at pH 7.5, beneath a single G-actin monomer, would, on average, have eight positive charges and be able to neutralize the $-7e$ charge of the G-actin monomer. A combination of an overall reduction in charge of the monomers via surrounding lipids and increased actin concentration though two-dimensional confinement with access to monomers from solution may then allow polymerization to occur.

Simulations of bulk polymerization have previously shown the most critical step in the nucleation process is the formation of a trimer, which has a large dissociation rate constant (26). The simulations predict that a nucleation pathway of a longitudinal dimer followed by trimer formation is >30-fold more favorable than from cross-filament dimer to trimer. Applying this scheme of polymerization to charged lipid bilayers in which monomers are in or close to the orientation required for longitudinal dimer formation enhances the potential to polymerize in non-polymerizing bulk conditions. This potential is further enhanced by the effect that adsorption at the membrane surface will lead to locally higher concentrations than in the bulk. The third monomer required to form the trimer could come directly from the solution (Fig. 7 *A*). In the trimer state, the association and dissociation rate constants are approximately equal to that of a full filament and thus form the critical nucleus. Polymerization from then on could continue via monomer two-dimensional diffusion on the membrane or three-dimensional diffusion from the bulk.

To gain insight into the significance of the contributions to polymerization from bulk three-dimensional diffusion and two-dimensional diffusion of lipid bound monomers, we can model each process based on the probability that a monomer arrives at the right angular orientation (Prot) in a given characteristic time ($\tau = R^2/2d\,D_d$). This characteristic time between arrival of monomers separated by a mean distance R (estimated via concentration c where $R \approx c^{-1/3}$ in three dimensions and $c^{-1/2}$ in two dimensions)

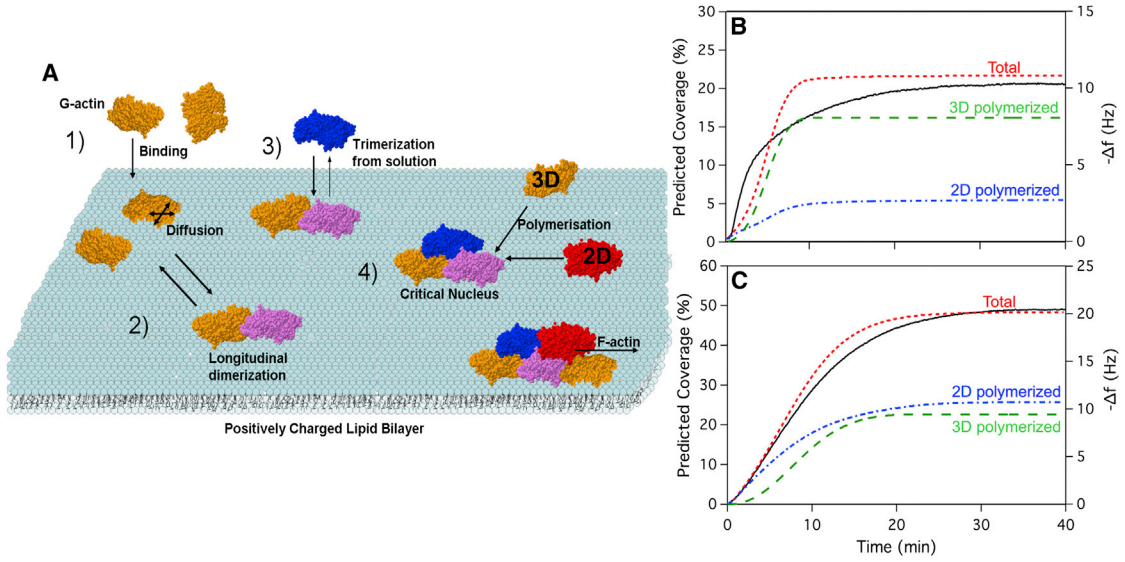

FIGURE 7 (*A*) Schematic description of the surface-induced self-assembly of G-actin into filaments on a positively charged lipid membrane: (*1*), monomeric actin binds to the membrane in a flat orientation where it diffuses at a rate that is dependent on the lipid mobility; (*2*), in-plane dimers form via diffusional collision; (*3*), G-actin from solution binds to form a trimer; and (*4*), trimer forms critical nucleus from which polymerization can occur via addition from solution and/or adsorbed diffusion. Model for growth via two-dimensional surface diffusion (*dash-dot*), or via addition from three-dimensional bulk phase (*long dash*) and total actin bound (*dash*) on gel-phase (*B*) and fluid-phase (*C*) bilayers as a function of time. The experimentally obtained data, from QCM-D, are shown (*solid lines*) in each case and represent actin binding to 4:1 DPPC/EDPPC and 4:1 DOPC/DOTAP bilayers. To see this figure in color, go online.

is set by the diffusion constant D_d (in d dimensions). The rate of polymerization can then be estimated as

$$k_{\text{on}} = \frac{P_{\text{rot}}}{\tau} e^{-\frac{\Delta G}{k_B T}}, \quad (1)$$

where ΔG describes the energy barrier once monomers have adsorbed. The charged membrane can be expected to remove the Coulomb barrier, which would be present for free monomers in solution. Table S1 in the Supporting Material shows the estimated arrival times, rotational probabilities, and energy barriers for polymerization in two and three dimensions. Assuming that the adsorbed monomers are at or close to the correct polar angle for interaction, only a small rotational barrier ΔG_{rot} needs to be overcome to tilt the monomer into or out of the membrane. This leads to the following capture rates:

$$k_{2d} = \frac{4 D_{2d} C_{2d}}{2\pi} \exp\left(-\frac{\Delta G_{3d} + \Delta G_{\text{rot}}}{k_B T} + \frac{q^2 e^{-\frac{r^*}{\lambda_D}}}{4\pi\epsilon r^* k_B T} \right), \quad (2)$$

$$k_{3d} = \frac{6 D_{3d} c^{2/3}}{4\pi} e^{-\frac{\Delta G_{3d}}{k_B T}}, \quad (3)$$

where the diffusion rate in three dimensions is 50 $\mu m^2/s$ (3) and ΔG_{rot} is approximated as 0.5 kcal/mol based on previous theoretical estimations (43). ΔG_{3d} is estimated as 3.5 kcal/mol in reasonable agreement with previous models (26). For the two-dimensional monomer diffusion rates we use 2.2 $\mu m^2/s$ for fluid-phase bilayers, as determined by TIRF microscopy (see Fig. S1), and for the gel phase we use the diffusion rate of the lipids (0.004 $\mu m^2/s$) as determined via FRAP experiments (see Fig. S5). Assuming irreversible adsorption to the membrane through diffusive flux (J_{ext}), we can model the contributions from bulk and surface diffusion to the surface actin concentration with time,

$$\frac{dc}{dt} = J_{\text{ext}}(1-\phi)c_1 - k_{2D}(c_1)\sum_{j=1}^{N-1} c_j - k_{3D} c_{3D}^{\frac{2}{3}}(1-\phi)c_1, \quad (4)$$

$$\frac{dc_j}{dt} = k_{2D}(c_1)c_1 c_{j-1} - k_{3D} c_{3D}^{\frac{2}{3}}(1-\phi)c_{j-1} \; (j = 2 \ldots N), \quad (5)$$

where c_j represents the concentration of aggregates of j. We also assume monomers can only adsorb where there is no actin giving a rise to the $(1-\phi)$ term, where the area fraction of free sites is given by

$$\phi(t) = a\sum_{i=1}^{N} n c_n(t), \quad (6)$$

where a is the area per monomer. Solving Eqs. 4 and 5 numerically with time, for $j = 2 \ldots 200$ for the gel and fluid systems (Fig. 7, *B* and *C*), we can model the results expected from QCM-D. The model predicts that for gel-phase bilayers, $D = 0.002$ $\mu m^2/s$, 75% of the actin is polymerized by additional actin arriving directly from the

bulk phase with 25% contribution from surface diffusion. By changing the diffusion coefficient to represent the fluid phase, $D = 2.2\ \mu m^2/s$, our model suggests that polymerization is initially dominated by monomers arriving by two-dimensional diffusion at the membrane but, over time, as more filaments are established, the three-dimensional component plays an increasing role, eventually leading to almost equal contributions from two and three dimensions (Fig. 7 *C*). These results show that controlling the membrane viscosity offers a simple but important route for controlling the morphology of the actin structures produced.

CONCLUSIONS

Our results show that lateral diffusion of the G-actin/cationic lipid complexes determines the degree and rate of actin polymerization with higher diffusion coefficients, increasing both rate and total amount of actin polymerized. QCM-D and AFM data show that G-actin has no interaction with neutral DOPC bilayers. The lipid charge required to induce polymerization depends on the membrane phase due to differences in lipid density and ability to change leaflet asymmetries. Fluid bilayers are known to have lipid leaflet distributions influenced by the charge presented by the support surface, thus leading to a reduced charge at the exposed monolayer/ambient interface. The denser gel-phase bilayers, which have much slower rates of lipid flip-flop, are expected to be more symmetric and thus require less total charge lipid in the membrane to promote polymerization. Investigating single-filament growth dynamics through time-lapse AFM has revealed linear filament polymerization, as is observed with monomer addition from the bulk (three-dimensional) in the case of gel-phase systems. Further, pH provides an additional handle on controlling the rates of nucleation and polymerization as well as the total amount of actin polymerized. In addition to providing insight into polymerization processes, this work provides a simple two-step method to creating a stable two-dimensional actin network membrane substrate. The benefits of this system come from the ability to control coverage and not require bulk polymerization, phalloidin, or additional linker proteins. This could therefore be useful for various applications requiring site-localized self-assembly or directed growth.

SUPPORTING MATERIAL

Five figures, one table, four movies, and supplemental information are available at http://www.biophysj.org/biophysj/supplemental/S0006-3495(13)01135-1.

We gratefully acknowledge the financial sponsorship from the Engineering and Physical Sciences Research Council under grant Nos. EP/I000623/1 and EP/J017566/1.

REFERENCES

1. Laliberte, A., and C. Gicquaud. 1988. Polymerization of actin by positively charged liposomes. *J. Cell Biol.* 106:1221–1227.
2. Pollard, T. D., and G. G. Borisy. 2003. Cellular motility driven by assembly and disassembly of actin filaments. *Cell.* 112:453–465.
3. Renault, A., P.-F. Lenne, …, F. Amblard. 1999. Surface-induced polymerization of actin. *Biophys. J.* 76:1580–1590.
4. Stricker, J., T. Falzone, and M. L. Gardel. 2010. Mechanics of the F-actin cytoskeleton. *J. Biomech.* 43:9–14.
5. Le Clainche, C., and M. F. Carlier. 2008. Regulation of actin assembly associated with protrusion and adhesion in cell migration. *Physiol. Rev.* 88:489–513.
6. Khurana, S., and S. P. George. 2011. The role of actin bundling proteins in the assembly of filopodia in epithelial cells. *Cell Adhes. Migr.* 5:409–420.
7. Mooseker, M. S., and L. G. Tilney. 1975. Organization of an actin filament-membrane complex. Filament polarity and membrane attachment in the microvilli of intestinal epithelial cells. *J. Cell Biol.* 67:725–743.
8. Patolsky, F., Y. Weizmann, and I. Willner. 2004. Actin-based metallic nanowires as bio-nanotransporters. *Nat. Mater.* 3:692–695.
9. Okamoto, A., K. Tanaka, and I. Saito. 2004. DNA logic gates. *J. Am. Chem. Soc.* 126:9458–9463.
10. Takatsuki, H., H. Tanaka, …, E. R. Blough. 2011. Transport of single cells using an actin bundle-myosin bionanomotor transport system. *Nanotechnology.* 22:245101.
11. Wong, G. C., J. X. Tang, …, C. R. Safinya. 2000. Hierarchical self-assembly of F-actin and cationic lipid complexes: stacked three-layer tubule networks. *Science.* 288:2035–2039.
12. Henry, E., A. Dif, …, F. Artzner. 2011. Crystallization of fluorescent quantum dots within a three-dimensional bio-organic template of actin filaments and lipid membranes. *Nano Lett.* 11:5443–5448.
13. Barfoot, R. J., K. H. Sheikh, …, S. D. Evans. 2008. Minimal F-actin cytoskeletal system for planar supported phospholipid bilayers. *Langmuir.* 24:6827–6836.
14. Shi, D., A. V. Somlyo, …, Z. Shao. 2001. Visualizing filamentous actin on lipid bilayers by atomic force microscopy in solution. *J. Microsc.* 201:377–382.
15. Yamamoto, D., N. Nagura, …, T. Ando. 2009. Streptavidin 2D crystal substrates for visualizing biomolecular processes by atomic force microscopy. *Biophys. J.* 97:2358–2367.
16. Bosk, S., J. A. Braunger, …, C. Steinem. 2011. Activation of F-actin binding capacity of ezrin: synergism of PIP_2 interaction and phosphorylation. *Biophys. J.* 100:1708–1717.
17. Sengupta, K., L. Limozin, …, E. Sackmann. 2006. Coupling artificial actin cortices to biofunctionalized lipid monolayers. *Langmuir.* 22:5776–5785.
18. Pontani, L.-L., J. van der Gucht, …, C. Sykes. 2009. Reconstitution of an actin cortex inside a liposome. *Biophys. J.* 96:192–198.
19. Kouyama, T., and K. Mihashi. 1981. Fluorimetry study of *n*-(1-pyrenyl)iodoacetamide-labeled F-actin. Local structural change of actin protomer both on polymerization and on binding of heavy meromyosin. *Eur. J. Biochem.* 114:33–38.
20. Kuhn, J. R., and T. D. Pollard. 2005. Real-time measurements of actin filament polymerization by total internal reflection fluorescence microscopy. *Biophys. J.* 88:1387–1402.
21. Lehto, T., M. Miaczynska, …, F. Severin. 2003. Observing the growth of individual actin filaments in cell extracts by time-lapse atomic force microscopy. *FEBS Lett.* 551:25–28.
22. Pardee, J. D., and J. A. Spudich. 1982. Purification of muscle actin. *In* Methods in Enzymology, Vol. 85, Part B Elsevier, Dordrecht, The Netherlands, pp. 164–181.
23. Smith, P. K., R. I. Krohn, …, D. C. Klenk. 1985. Measurement of protein using bicinchoninic acid. *Anal. Biochem.* 150:76–85.

24. Wang, H., R. C. Robinson, and L. D. Burtnick. 2010. The structure of native G-actin. *Cytoskeleton (Hoboken).* 67:456–465.

25. Taylor, K. A., and D. W. Taylor. 1992. Formation of 2-D paracrystals of F-actin on phospholipid layers mixed with quaternary ammonium surfactants. *J. Struct. Biol.* 108:140–147.

26. Sept, D., and J. A. McCammon. 2001. Thermodynamics and kinetics of actin filament nucleation. *Biophys. J.* 81:667–674.

27. Callan-Jones, A. C., R. A. Pelcovits, …, G. B. Loriot. 2006. Simulation and visualization of topological defects in nematic liquid crystals. *Phys. Rev. E Stat. Nonlin. Soft Matter Phys.* 74:061701.

28. Holmes, K. C., D. Popp, …, W. Kabsch. 1990. Atomic model of the actin filament. *Nature.* 347:44–49.

29. Carlier, M. F., D. Pantaloni, and E. D. Korn. 1986. Fluorescence measurements of the binding of cations to high-affinity and low-affinity sites on ATP-G-actin. *J. Biol. Chem.* 261:10778–10784.

30. Tang, J. X., and P. A. Janmey. 1996. The polyelectrolyte nature of F-actin and the mechanism of actin bundle formation. *J. Biol. Chem.* 271:8556–8563.

31. Richter, R. P., N. Maury, and A. R. Brisson. 2005. On the effect of the solid support on the interleaflet distribution of lipids in supported lipid bilayers. *Langmuir.* 21:299–304.

32. Pan, J., S. Tristram-Nagle, …, J. F. Nagle. 2008. Temperature dependence of structure, bending rigidity, and bilayer interactions of dioleoylphosphatidylcholine bilayers. *Biophys. J.* 94:117–124.

33. Nagle, J. F., and S. Tristram-Nagle. 2000. Structure of lipid bilayers. *Biochim. Biophys. Acta.* 1469:159–195.

34. Andrianantoandro, E., L. Blanchoin, …, T. D. Pollard. 2001. Kinetic mechanism of end-to-end annealing of actin filaments. *J. Mol. Biol.* 312:721–730.

35. Popp, D., A. Yamamoto, and Y. Maéda. 2007. Crowded surfaces change annealing dynamics of actin filaments. *J. Mol. Biol.* 368: 365–374.

36. Pollard, T. D., D. Bhandari, …, H. G. Zot. 1993. Direct visualization by electron microscopy of the weakly bound intermediates in the actomyosin adenosine triphosphatase cycle. *Biophys. J.* 64:454–471.

37. Wang, F., R. V. Sampogna, and B. R. Ware. 1989. pH dependence of actin self-assembly. *Biophys. J.* 55:293–298.

38. Crevenna, A. H., N. Naredi-Rainer, …, R. Wedlich-Söldner. 2013. Electrostatics control actin filament nucleation and elongation kinetics. *J. Biol. Chem.* 288:12102–12113.

39. Tanford, C., and J. G. Kirkwood. 1957. Theory of protein titration curves. I. General equations for impenetrable spheres. *J. Am. Chem. Soc.* 79:5333–5339.

40. Tanford, C., and R. Roxby. 1972. Interpretation of protein titration curves. Application to lysozyme. *Biochemistry.* 11:2192–2198.

41. Shire, S. J., G. I. H. Hanania, and F. R. N. Gurd. 1974. Electrostatic effects in myoglobin. Hydrogen ion equilibria in sperm whale ferrimyoglobin. *Biochemistry.* 13:2967–2974.

42. Matthew, J. B. 1985. Electrostatic effects in proteins. *Annu. Rev. Biophys. Biophys. Chem.* 14:387–417.

43. Tamura, A., and P. L. Privalov. 1997. The entropy cost of protein association. *J. Mol. Biol.* 273:1048–1060.